scientific reports

Check for updates

OPEN

Bayesian toxicokinetic modeling of subcellular partitioning in grass carp exposed to copper nanoparticles and its implication for detoxification

Hsing-Chieh Lin[1], Yu-Lin Tsai[2], Bing-Ru Hsiao[2], Li-Hsuan Li[2], Hsueh-Han Hsieh[2,3], Tzu-Hu Liu[2], Chong-Wei Li[1] & Wei-Yu Chen[1]✉

Understanding the accumulation mechanisms and particle-specific effects of nanoparticles in aquatic organisms is crucial for assessing ecotoxicological risks of nanomaterials. The aim of this study is to evaluate the influence of copper nanoparticles (CuNPs) particle size (40–60 nm and 60–80 nm) on the subcellular partitioning kinetics of Cu in grass carp (*Ctenopharyngodon idellus*) tissues, utilizing a Bayesian two-compartment toxicokinetic (TK) model. Fish were exposed to these CuNPs at concentrations of 0.03, 0.1, and 0.3 μg mL^{-1} for 10 days. Bayesian Markov chain Monte Carlo (MCMC) simulation enabled stochastic estimation of uptake (k_{uA}), detoxification (k_d), and elimination (k_e) rate constants, along with uncertainty quantification. Results showed that smaller CuNP particle sizes affect greater Cu accumulation in the liver and kidney at low to moderate concentrations than at high concentrations, likely due to particle aggregation at higher exposure level. Bayesian TK model revealed tissue-specific kinetic profiles, larger CuNP exhibited faster uptake, while smaller particle enhanced higher detoxification rates, especially in the liver and intestine. These results showed how particle size and concentration affect Cu subcellular fate through dynamic detoxification mechanisms. In conclusion, Bayesian MCMC subcellular partitioning TK model advances the understanding of particle size effects in aquatic nanotoxicology, emphasizing the importance of considering particle characteristics and exposure levels in assessing biological responses and environmental risks of exposure to CuNPs in aquatic ecosystems.

Keywords Copper nanoparticles, Particle size, Subcellular partitioning, Bayesian inference, Toxicokinetic model, Detoxification

Copper nanoparticles (CuNPs) exhibit modulated characteristics dependent on their shape, particle size, and density[1]. Their high specific surface area and reaction activity foster novel benefits across various sectors, including semiconductor technology, biomaterials, energy production, and environmental technology[2]. The extensive production of CuNPs leads to their discharge into aquatic environments through industrial effluents, antimicrobial waste from domestic sources, and agricultural practices. CuNPs come into direct contact with receiving water environments and aquatic organisms upon release. Adam et al.[3] estimated that surface waters in Europe receive up to 23% of the total nanometal burden across various environmental compartments, including air, sludge-treated soil, surface water, natural and urban soil, and subsurface environments. Predictions from the NanoFate model show that the release of CuNPs into freshwater environments would increase dissolved Cu concentrations from 1 to 100 ng L^{-1}, primarily due to the dissolution and aggregation of CuNPs[4]. Furthermore, CuNPs release Cu in nanoparticles or ionic form[5,6], both of which have the potential to accumulate in aquatic organisms, raising concerns about potential risks to ecological health posed by CuNPs.

[1]Department of Ecology and Environmental Resources, National University of Tainan, Tainan, Taiwan. [2]Department of Biomedical Science and Environmental Biology, Kaohsiung Medical University, Kaohsiung, Taiwan. [3]Department of Oceanography, National Sun Yat-Sen University, Kaohsiung, Taiwan. ✉email: f96622016@ntu.edu.tw; wychen@mail.nutn.edu.tw

The transport, accumulation, and toxicity of nanomaterials are dependent on factors such as size, shape, surface reactivity, crystallinity, aggregation, and dissolution[6–8]. In particular, particle size is directly correlated with key factors influencing nanoparticle fate, bioaccumulation, and toxicological behavior[9,10]. While numerous studies have observed that organisms exposed to smaller metallic nanoparticles tend to accumulate metal more readily[11,12], contrasting evidence suggests that larger particle sizes result in greater metal accumulation[10,13]. However, it remains unclear whether the size of metallic nanoparticles directly influences metal accumulation, and most research on particle size-dependent metal accumulation in aquatic organisms has focused on silver nanoparticle[10–13]. The current limited understanding of nanoeffects arises from the relationship between particle size and its impact on particle characteristics, which ultimately influence toxicokinetics and nanotoxicity. Burello and Worth[14] emphasized the importance of considering the size effects and nanoparticle characteristics in nanotoxicological studies. Nevertheless, few studies have addressed the dynamic kinetic of partitioning into the metabolically active pool (MAP) and the metabolically detoxified pool (MDP).

The presence of metallic nanoparticles at the subcellular level plays a crucial role in determining the processes of nanotoxicity in aquatic organisms, influencing both their toxicity and detoxification processes[15,16]. The effectiveness of activating and detoxifying metallic nanoparticles depends on the threshold concentration of subcellular partitioning in both the MAP and the MDP of the affected organism[15,17]. Furthermore, subcellular partitioning allows a more accurate assessment of the metal load and its potential harmful effects on the organism[18,19], thus enhancing the overall knowledge gained from the research in this field. It is crucial to quantitatively assess the absorption and depuration kinetics of metallic nanoparticles at the subcellular level, as this can significantly improve the evaluation and prediction of metal accumulation and associated toxicity, which may induce cellular damage and generate reactive oxygen species[20,21]. However, compartmentalized subcellular partitioning into the MAP and MDP is rarely studied in terms of absorption and depuration kinetics[22]. However, there is currently a lack of subcellular toxicokinetic models for metallic nanoparticles. One of the few studies to utilize such models evaluated the impact of cadmium nanoparticles on bivalves[15]. Understanding the toxicokinetics of CuNPs at the subcellular level reveals mechanistic insight and provides critical parameters for predictive models that can support environmental risk assessments and enhance monitoring strategies.

Insufficient subcellular toxicokinetic data on the size-dependent effects of metallic nanoparticles is characterized by uncertainty and variability, changes that Bayesian analysis can address to optimize model simulations[23,24]. By integrating prior knowledge and experimental data, Bayesian analysis (i.e., Markov chain Monte Carlo (MCMC) techniques) facilitates the optimization of parameterization, providing posterior distributions rather than point estimates and extending the potential for uncertainty analysis[24,25]. Furthermore, Bayesian MCMC methods provide a robust framework for evaluating toxicokinetic (TK) model structures, incorporating multiple datasets and a wide range of parameter values. As a result, this approach could significantly contribute to elucidating the factors that influence the toxicokinetics of nanoparticles[26]. These advantages enhance the reliability of toxicokinetic modeling by capturing parameter uncertainty and biological variability to support scenario-based modeling efforts relevant to metallic nanoparticle exposures in aquatic environments.

This study hypothesizes that particle size influences the subcellular partitioning kinetics of Cu in the MAP and MDP in aquatic organisms following CuNP exposure. To test this hypothesis, we focused on examining Cu subcellular partitioning in tissues of grass carp (*Ctenopharyngodon idellus*). Additionally, we aimed to develop a subcellular partitioning TK model incorporating Bayesian analysis to estimate size-dependent CuNP toxicokinetic parameters. The integrated approach provides a quantitative framework for improving the understanding of CuNP behavior in aquatic organisms, addressing environmental risk assessment and management of nanoparticles.

Materials and methods

Nanoparticle solutions and characterization

The particle sizes of 40–60 nm and 60–80 nm copper nanopowder used were purchased from Sigma-Aldrich (> 99.5% purity). The 1000 mg L^{-1} CuNP stock solutions were prepared by dispersing 40 mg of Cu nanopowder in 40 mL of ultrapure water (Millipore) by an ultrasonic homogenizer (Hielscher UP50H) to avoid aggregating. Then, the stocks were ultrasonicated with a 30 kHz ultrasonic frequency and 100% amplitudes for at least 30 min to increase dispersion before the dosing event. We put 10 µL of drop solution (100 mg L^{-1} CuNPs) onto a 200-mesh copper grid and dried it overnight at room temperature for particle image analysis. The image analysis of the CuNPs by transmission electron microscopy (Hitachi HT7700) revealed the morphology, aggregation, and particle size in ultrapure water (Fig. S1). The diameters of the 40–60 nm and 60–80 nm individual CuNPs were approximately 40 nm and 60 nm, respectively. The CuNPs appeared spherical, and particle size distribution with a mean particle size of 72.548 ± 68.305 nm (n = 218) of 40–60 nm, and a mean particle size of 86.182 ± 61.016 nm (n = 151) for 60–80 nm (both including aggregates). The mean sizes of aggregates were 169.997 ± 74.973 nm (range: 81.562–357.865 nm; n = 53) for 40–60 nm and 163.810 ± 73.576 nm (range: 86.701–403.392 nm; n = 42) for 60–80 nm.

Experimental design

Grass carp (*Ctenopharyngodon idellus*) were obtained from Yuantai Fish Hatchery in Changhua County, Taiwan. Juvenile fish (body weight: 13.45 ± 8.69 g; body length: 10.95 ± 2.20 cm) were acclimated in 50-L tanks filled with tap water dechlorinated at a temperature of 26–28 °C, pH 8.2 ± 0.04, and dissolved oxygen 7.8 ± 0.2 mg L^{-1} in a 12-hour light-dark cycle for 14 days before the exposure tests. The water quality of Kaohsiung tap water was as follows: total hardness 158.83 mg L^{-1}, alkalinity 104.15 mg L^{-1}, total dissolved solids 296.67 mg L^{-1}, ammonia was ND, and background Cu level < 0.01 mg L^{-1}. The fish were fed commercial fish pellets (2.0 mm) daily at a

rate of 1% of their gross body weight during the acclimation period, but they were intentionally not fed for 24 h before and during the test to minimize the intake of fecal debris and Cu from the food.

Fish were exposed to CuNPs on controlled laboratory conditions with two particle sizes (40–60 nm and 60–80 nm) and three concentrations (0.03 μg mL^{-1}, 0.1 μg mL^{-1}, and 0.3 μg mL^{-1}) for 10 days. The particle sizes were selected based on CuNP size-dependent toxicity in rat neurons[27], and exposure concentrations were adjusted with reference to previous CuNP bioaccumulation studies in fish[28,29]. Thirty-two fish in each treatment group were randomly allocated into two tanks. All treatments were performed in 50-L water volume within indoor rectangular fiberglass aquaria (60 × 37 × 36 cm), and a 50% water change, along with re-dosing, was performed every two days. To avoid the potential influence of dietary Cu accumulation, fish were not fed during the 10-day exposure period. The duration chosen to prevent starvation-related physiological stress, as grass carp fingerlings can survive without food for at least 15 days[30] Similar experimental durations have been used in CuNP accumulation studies[28,31]. Five fish were sampled at 0, 2, 4, 6, 8, and 10 days to analyze subcellular copper partitioning in liver, kidney, and intestine. The grass carps were anesthetized with benzocaine hydrochloride solution during the sampling. The dissected intestine, kidney, and liver samples were cleaned with ultrapure water and freeze-stored at − 80 °C in the dark until analyzed. No mortality was observed during the experiment. The fish were euthanized using benzocaine hydrochloride solution at 250 mg L^{-1}. The procedures for the exposure bioassays were approved by the Ethical and Scientific Committee of Kaohsiung Medical University. All experimental procedures were conducted in accordance with relevant guidelines and regulations. The exposure experiments were performed in accordance with the OECD Test Guideline 305 for bioaccumulation in fish. This study was reported in accordance with the ARRIVE guidelines[32].

Subcellular partitioning and chemical analysis

A modified method based on Wallace et al.[20] and Geffard et al.[33] was used to homogenize tissues and separate subcellular fractions by centrifugation. Five subcellular partitioning were isolated: metal-rich granules, organelles, heat-denatured proteins, metallothionein-like protein, and cellular debris. The separated subcellular fractions were analyzed for Cu residues. The frozen tissues (stored at − 80 °C) was transferred into a pre-weighted 2-mL tube. After weighing, the tissue was mixed with lysis buffer (10 mM Tris-HCl and 5 mM 2-ME) in an ice bath. The mixture was homogenized using a homogenizer (Tissue-Tearor Modle 98570, Dremel) at medium speed. The tissue-to-lysis buffer ratio was 1:4. The homogenized tissue was first centrifuged at 1500 g at 4 °C for 30 min (Micro 17TR, Hanil, Korea) to obtain a pellet (P1) and supernatant (S1). The pellet (P1) was suspended in 1 N NaOH (half volume of lysis buffer) and heated at 100 °C for 2 min before adding ultrapure water (half volume of lysis buffer) to the pellet and heating at 65 °C for 60 min. To separate the metal-rich granules (P2) and cellular debris (S2), the mixture was re-centrifuged at 10,000 g at 4 °C for 10 min. The supernatant 1 (S1) was transferred to a polycarbonate bottle (Beckman Coulter, USA) and re-centrifuged at 100,000 g at 4 °C for 60 min by ultracentrifuge (Optima L-90 K preparative ultracentrifuge, Beckman Coulter, USA; Rotor: Type 70.1 Ti) to separate the organelles (P3) and cytosol (S3). The cytosol (S3) was heated at 80 °C for 10 min and cooled at 0 °C for 60 min. After denaturation, the cytosol was re-centrifuged at 30,000 g at 4 °C for 20 minutes to separate the final pellet (P4, heat-denatured protein) and supernatant (S4, metallothionein-like protein).

Both the pellet and supernatant samples were digested in 1 mL HNO_3 at 80 °C for 6 h and Cu analysis was conducted by a Flame Atomic Absorption Spectrometer (Perkin-Elmer PinAAcle 500, USA). Analytical quality control was ensured with certified reference materials (Dogfish muscle, DORM-2, National Research Council, Canada). The limit of detection was 20 μg g^{-1} for tissues samples and 20 μg L^{-1} for water samples, with a recovery value of 102.8 ± 22.8%.

Bayesian two-compartmental toxicokinetic model

The two-compartment toxicokinetic model (Fig. 1), modified from the theoretical framework of metal accumulation proposed by Rainbow[34], was applied to describe the time-course Cu concentrations during CuNP exposure. Based on the metal subcellular distribution concept, Cu can be accumulated and distributed in two compartments: the metabolically active pool (MAP) and the metabolically detoxification pool (MDP). The MAP comprises the toxic actions that occur in organelles and heat-denatured proteins, and the MDP comprises the defective responses in metallothionein and metal-rich granules. Metallothionein proteins are rich in cysteine,

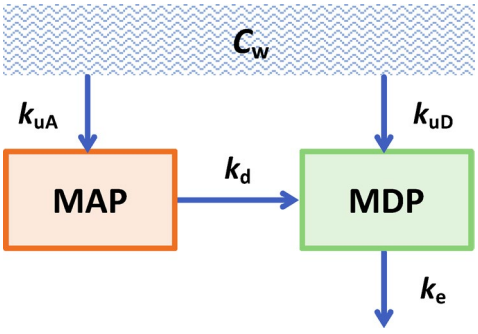

Fig. 1. Schematic of a two-compartmental toxicokinetic model illustrating CuNP distribution among subcellular partitioning in grass carp.

comprising over 30% of the total amino acid residues, and have a high affinity for metal cations[35]. Previous studies have shown that metallothionein-like proteins can be rapidly induced by exposure to ambient metals, particularly copper, zinc, and cadmium, and that these proteins subsequently bind specifically to incoming metals[36–38], without passing through the MAP, highlighting the role of metallothionein-like proteins in the cellular response exposure. In this model, we incorporated direct uptake of CuNPs from water into both MDP and MAP. This assumption accounts for the simultaneous accumulation of Cu in both pools: the MAP where Cu supports metabolic and enzymatic function, and MDP where metals are sequestered for detoxification. Based on metabolic requirements for essential metals, Cu accumulates in the MAP to support the enzyme requirement. When metal levels exceed metabolic needs, they are transferred to the MDP for detoxified storage, and elimination of accumulated metal occurs primarily in MDP[34]. For example, copper accumulates in metal-rich granules and is eliminated detoxified through the cell cycle in alimentary tract[39]. The processes of Cu kinetics within the grass carps following exposure to CuNPs were assumed to include the influx from water into both the MAP and MDP, the detoxifying transfer from the MAP to the MDP, and the efflux occurring in the MDP. The mathematical equations for these processes are as follows:

$$\frac{dC_{\mathrm{MAP}}(t)}{dt} = k_{\mathrm{uA}} C_{\mathrm{W}} - k_{\mathrm{d}} C_{\mathrm{MAP}}$$

$$\frac{dC_{\mathrm{MDP}}(t)}{dt} = k_{\mathrm{uD}} C_{\mathrm{W}} + k_{\mathrm{d}} C_{\mathrm{MAP}} - k_{\mathrm{e}} C_{\mathrm{MDP}}$$

where $C_{\mathrm{MAP}}(t)$ and $C_{\mathrm{MDP}}(t)$ are the concentrations of Cu distributed in the MAP and the MDP (μg Cu g^{-1} tissue), respectively, and C_{w} is the CuNP concentration in solution (μg CuNP mL^{-1} water). k_{uA} and k_{uD} are the uptake rate of the MAP and the MDP compartments (mL g^{-1} day^{-1}), respectively, k_{e} is the elimination rate (day^{-1}), and k_{d} is the detoxification rate (day^{-1}).

The toxicokinetic parameters, i.e., k_{uA}, k_{uD}, k_{e}, and k_{d}, for each exposure combination of CuNP concentrations and particle sizes were estimated and optimized using the Bayesian Markov chain Monte Carlo (MCMC) method. The main notion of Bayes' theorem for parameter estimation is to acquire the joint *posteriors*, which combined the data likelihood with the prior knowledge of the parameters. First, for the prior estimates, due to the lack of parametric information regarding subcellular partitioning in the literature, we used the Cu concentration data profiles and applied least-squares curve fitting with the Levenberg-Marquardt (LM) algorithm to obtain the means and standard deviations (SDs) of the parameters. The LM algorithm was implemented using OpenModel 2.4.2 software. The prior distributions for most parameters were assigned as log-normal distributions with a truncated setting, where the maximum value was set to ten times the mean. However, if the estimated SD was extremely larger than its mean, the prior distribution was set as a uniform distribution, ranging from 10^{-7} to 10, to provide considerable freedom in sampling spaces for testing. Subsequently, the likelihood of the data was assumed to be based on the variances of the concentration data.

To execute the MCMC algorithm, the Metropolis-Hastings (MH) algorithm was employed to combine the data likelihood and the prior distributions and to generate four Markov chains for obtaining posterior parametric estimates. The MCMC computation was implemented using MCSim software (version 6.1.0) within an R Studio interface. Each independent chain possessed 2,000 iterations, of which the first half were "burn-in," and the last half of those were used to examine the convergence and estimate the posterior distributions of the involved parameters. The estimated scale reduction ($\hat{R}$) established by Gelman and Rubin[40] was used to examine the convergence of the Markov chains. Values of $\hat{R}$ below 1.2 indicate that the chains have likely converged and the model results are considered stable.

Statistical analysis

We used the mean arctangent absolute percentage error (MAAPE) as the goodness-of-fit index to assess the model fitting performance. The calculated equation proposed by Kim and Kim[41] is as follows:

$$MAAPE = \frac{1}{n}\sum_{i=1}^{n} \arctan\left(\left|\frac{E_i - P_i}{E_i}\right|\right) \times 100\%$$

where E_i and P_i are the experimental and predicted values given by a particular time point *i*. Considering the range of the arctangent and referring to Moreno et al.[42], we determined that the acceptable level for model accuracy should be lower than 50%. This value reflects the average angular error between predicted and observed values, and a MAAPE below 50% is considered to indicate an acceptable predictive performance in similar biological modeling contexts.

Data were tested for normality, homogeneity of variance, and independence prior to statistical analyses. Statistical differences in Cu accumulation between small-sized and large-sized particle treatments, the MAP and the MDP, and exposure times on day 0 and day 10 were analyzed using the t-test when assumption were satisfied; otherwise, the Mann-Whitney U-test was used instead. The difference among the exposure concentrations was tested using the one-way ANOVA with Tukey's test. The Kruskal-Wallis test followed by the Dunn's post-hoc test was used when assumptions were not satisfied. A factor analysis of mixed data (FAMD), a type of principal component analysis (PCA) designed for datasets containing categorical variables, was used to examine the associations among the CuNP exposure concentrations, nanoparticle sizes, and the subcellular partitioning of Cu in the intestine, kidney, and liver during the 10-day exposure period. This PCA method was referred to in Rocha et al.[15]. Input factors included the concentration in the different subcellular fractions and their percentages to describe the subcellular partitioning. After obtaining the posterior parameters, a hierarchical

clustering on principal components (HCPC) approach was employed to evaluate the interrelatedness of the kinetic parameters, the exposure concentration and particle size. The standard processes of the HCPC approach were included in a FAMD followed by hierarchical clustering. The clustering was depicted by a dendrogram based on Ward's minimum variance method with calculating Euclidean distances. All FAMD and HCPC analysis in this study were conducted by R version 3.6.3 with the *FactoMineR*[43] (v2.4) and *factoextra* (v1.0.7)[44] packages. The significance level was set such that the *p*-value was less than 0.05.

Results

Tissue-specific subcellular partitioning kinetic parameters

The measured Cu concentrations in the MAP and the MDP of the livers, kidneys, and intestines of grass carps exposed to 0.03, 0.1, and 0.3 μg mL^{-1} CuNPs, with particle sizes ranging from 40 to 60 nm and 60–80 nm is presented in Fig. 2. Cu accumulation followed the order: liver > kidney > intestine, with concentrations generally increasing over time across all tissues. Cu concentrations measured at initial exposure and at the end of the 10-day exposure period revealed an overall increase in Cu concentration in both the MAP and MDP of all three tissues, with a few exceptions (Fig. S2). Specifically, no significant increase was observed in the MDP of livers for 60–80 nm CuNPs at 0.3 μg mL^{-1}, the MDP of the kidneys, and the 40–60 nm CuNPs at 0.3 μg mL^{-1} in the MAP

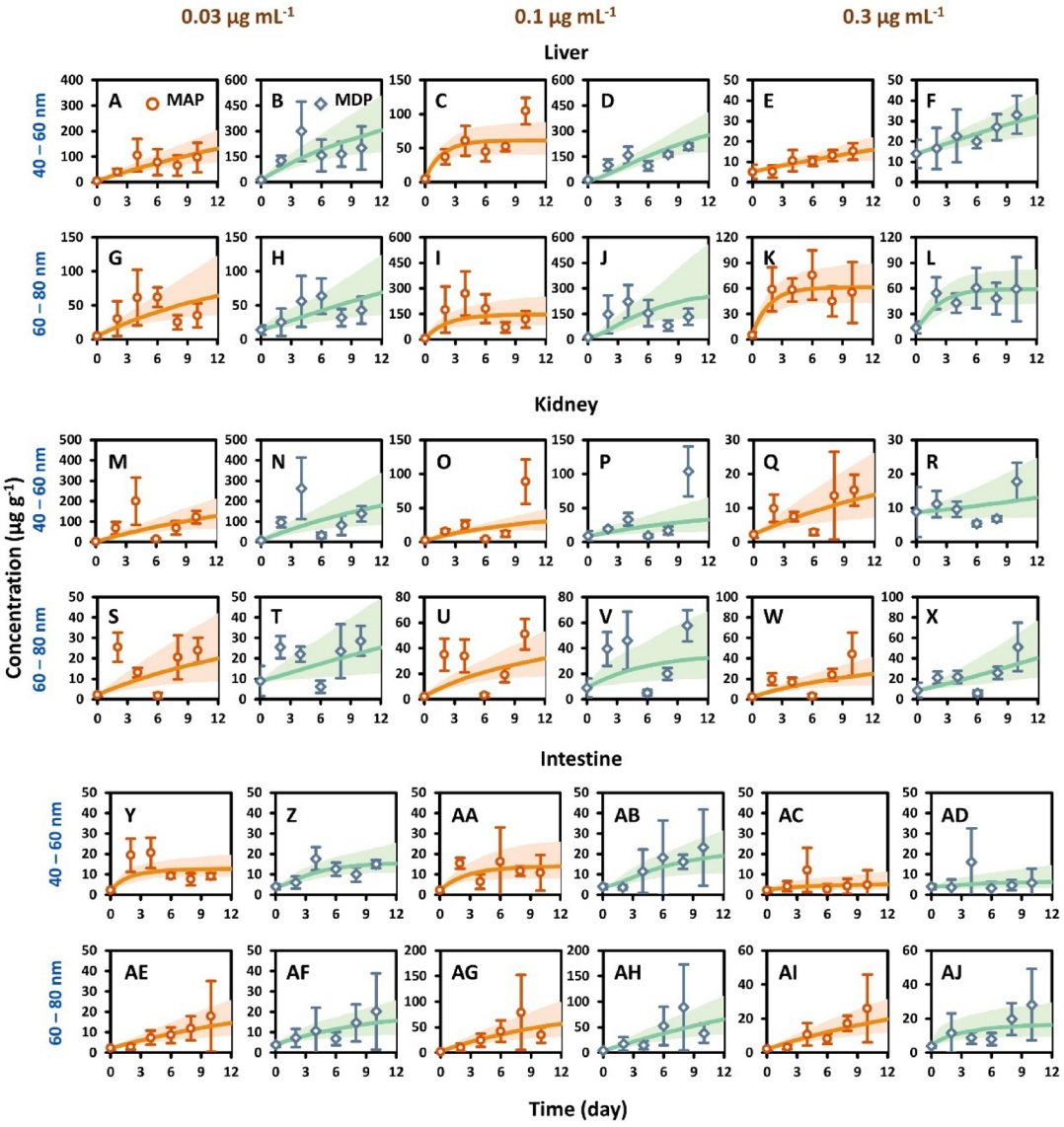

Fig. 2. Comparison of the observed time-course data (mean ± SD) to simulated concentrations in the metabolically active pool (MAP) and metabolically detoxified pool (MDP) of (**A**–**L**) liver, (**M**–**X**) kidneys and (**Y**–**AJ**) intestines in grass crap exposed to 0.03, 0.1, and 0.3 μg mL^{-1} CuNPs of 40–60 and 60–80 nm. Circular and diamond markers represent experimental data for MAP and MDP, respectively. Orange and green shaded areas with solid lines indicate simulated concentrations for MAP and MDP, respectively, along with 95% confidence intervals. Data are shown as mean ± SD; $n = 5$ unless noted (See Table S2 for condition with $n = 4$).

and MDP of the intestines (Fig. S2C, I, O). Although these cases showed no significant differences, a tendency toward the lowest accumulation was observed in the intestines under the highest exposure concentration of smaller particle size (40–60 nm at 0.3 μg mL^{-1}).

We applied the Bayesian two-compartment toxicokinetic model to fit the observed Cu concentrations in the MAP and the MDP of the livers, kidneys, and intestines following CuNP exposures, in order to estimate the kinetic parameters of MAP and MDP (Fig. 2). The model showed good model fitting performance, as indicated by MAAPE values, from most tissues and treatments (Fig. S3). However, exceptions were observed in the kidney exposed to 0.1 μg mL^{-1} (Fig. S3B), where higher MAAPE values were found for the MAP (40–60 nm: 56.96%) and for both the MAP and MDP (60–80 nm: 54.03% and 53.10%, respectively). The results revealed that Bayesian subcellular toxicokinetic modeling can be applied to predict accumulation, biological activity, and detoxification under environmentally relevant CuNP exposure scenarios.

The model predictions revealed a linear increase in Cu concentration in the MAP and MDP of livers exposed to the lowest and highest concentration of 40–60 nm CuNPs and the lowest concentration of 60–80 nm treatments (Fig. 2A, B, E–H) and in the kidneys throughout the exposure period for all treatments (Fig. 2M–X). In contrast, Cu accumulation in the intestines was slower, particularity at the highest concentration of 40–60 nm CuNPs (Fig. 2AC, AD). In general, Cu accumulation in the MAP reached equilibrium more quickly than in the MDP, particularly in the intestines and livers, suggesting limited toxicity concerns for CuNPs exposure. Furthermore, at the end of the exposure, the livers and intestines exhibited higher Cu accumulation in the MDP compared to the MAP, especially following exposure to smaller-sized CuNPs (liver: 0.1 μg mL^{-1} and 0.3 μg mL^{-1}; intestine: 0.03 μg mL^{-1}; Fig. S4). Across all tissues, Cu accumulation was higher in the MDP than in the MAP, particularly in the livers and intestines, emphasizing the role of detoxification in these tissues.

The convergence assessment confirmed that the estimated kinetic parameters met the criteria (Table S1, Fig. 3). The uptake rate constant for the MAP (k_{uA}) in all tissues decreased as the concentration of small particles increased (Fig. 3A–C). Similarly, k_{uA} in the kidneys also decreased with increasing concentrations of large-particle CuNPs (Fig. 3B). In addition, the uptake rate constant for MDP (k_{uD}) in the intestines declined with increasing concentration from both particle size treatments (Fig. 3F), whereas k_{uD} in the liver remained unaffected (Fig. 3D). When comparing the estimated kinetic parameters between MAP and MDP, we observed tissue-specific trends. In the livers, k_{uA} was quicker than the k_{uD} for the large particle treatment (Fig. 3A, D), whereas in the intestines, a quicker k_{uA} was observed for the small particle treatment (Fig. 3C, F).

Although smaller-sized CuNPs were associated with higher potential toxicity in the intestines, as indicated by $k_{uA} > k_{uD}$, the transfer rate from the MAP to the MDP for detoxification (k_d) was also quicker for the smaller particle exposures (0.41–0.57 day^{-1}) compared to the larger particle exposures (0.05–0.1 day^{-1}) (Fig. 3I). In the liver, both k_d and elimination rate constant (k_e) increased with increasing CuNP exposure concentration in the larger particle treatment, indicating enhanced detoxification and elimination (Fig. 3G, J). In contrast, the kidneys exhibited minimal differences k_d and k_e values between small and large particle treatments (Fig. 3H, K). These results suggest that the livers and intestines play critical roles in detoxification in response to CuNP exposure. Furthermore, exposure to larger particles is associated with greater liver detoxification and elimination stability than smaller particles. These subcellular partitioning kinetic parameters provide insights into tissue-specific detoxification processes and could be essential for developing further predictive models. However, a mechanistic model alone is not sufficient to fully elucidate the detoxification mechanisms. A more comprehensive understanding of nanoparticle detoxification at the cellular level could be achieved by incorporating biochemical biomarkers, such as metallothioneines, oxidative stress, and related enzymatic responses.

To compare k_{uA} and k_d, we first examined their correlation to assess whether these two parameters are independent, as the model structure suggests that k_{uA} and k_d may be correlated. We computed Pearson's correlation coefficients across various conditions. Strong correlations ($r > 0.7$) were observed in five specific cases: the intestine exposed to 40–60 nm CuNP at 0.03 and 0.3 μg mL^{-1}; the kidney exposed to 40–60 nm and 60–80 nm CuNP at 0.1 μg mL^{-1}; and the liver exposed to 60–80 nm CuNP at 0.3 μg mL^{-1} (Fig. S5). For most other combinations of tissues, exposure concentration, and particle size, the correlations were moderate to weak ($r < 0.7$). These findings indicate that individual parameter estimates remain interpretable despite some observed correlations.

Influence of particle size and concentration on subcellular accumulation

Figure 4 illustrates a comparison between the two particle sizes revealed that smaller-sized CuNPs had higher Cu accumulation than large-sized CuNPs under certain conditions: at the lowest concentration exposures in the MDP of the livers (Fig. 4A), in the MAP and the MDP of the kidneys (Fig. 4D), and at the moderate concentration exposure in the MDP of both livers and kidneys (Fig. 4B, E). However, at the highest exposure concentration, Cu accumulation was lower in the MAP and the MDP of the kidneys with smaller-sized CuNPs, and at moderate exposure concentration, it was a lower accumulation in the MAP of the intestines compared to the larger-sized CuNPs (Fig. 4F). These findings indicated that smaller-sized CuNPs generally led to higher Cu accumulation in the liver and kidneys. However, at the highest exposure concentration, CuNP exposure did not enhance Cu accumulation, particularly with smaller-sized CuNPs.

Cu accumulation in the MAP and the MDP of the tissues showed significant differences among exposure concentrations to CuNPs of the same particle size (Fig. 5), except in the intestines. For the smaller particle size (40–60 nm), the highest concentration exposure is associated with the lowest Cu accumulation in the livers (MAP: $p = 0.017$; MDP: $p = 0.017$, Fig. 5A), and the MAP and the MDP of the kidneys (MAP: $p = 0.0096$; MDP: $p = 0.013$, Fig. 5C). Conversely, for the larger particle size (60–80 nm), the highest accumulation in the MAP and the MDP of the livers (MAP: $p = 0.039$; MDP: $p = 0.032$, Fig. 5B) and the kidneys (MAP: $p = 0.012$; MDP: $p = 0.012$; Fig. 5D) was observed at the moderate exposure concentration. The results showed that, despite increasing

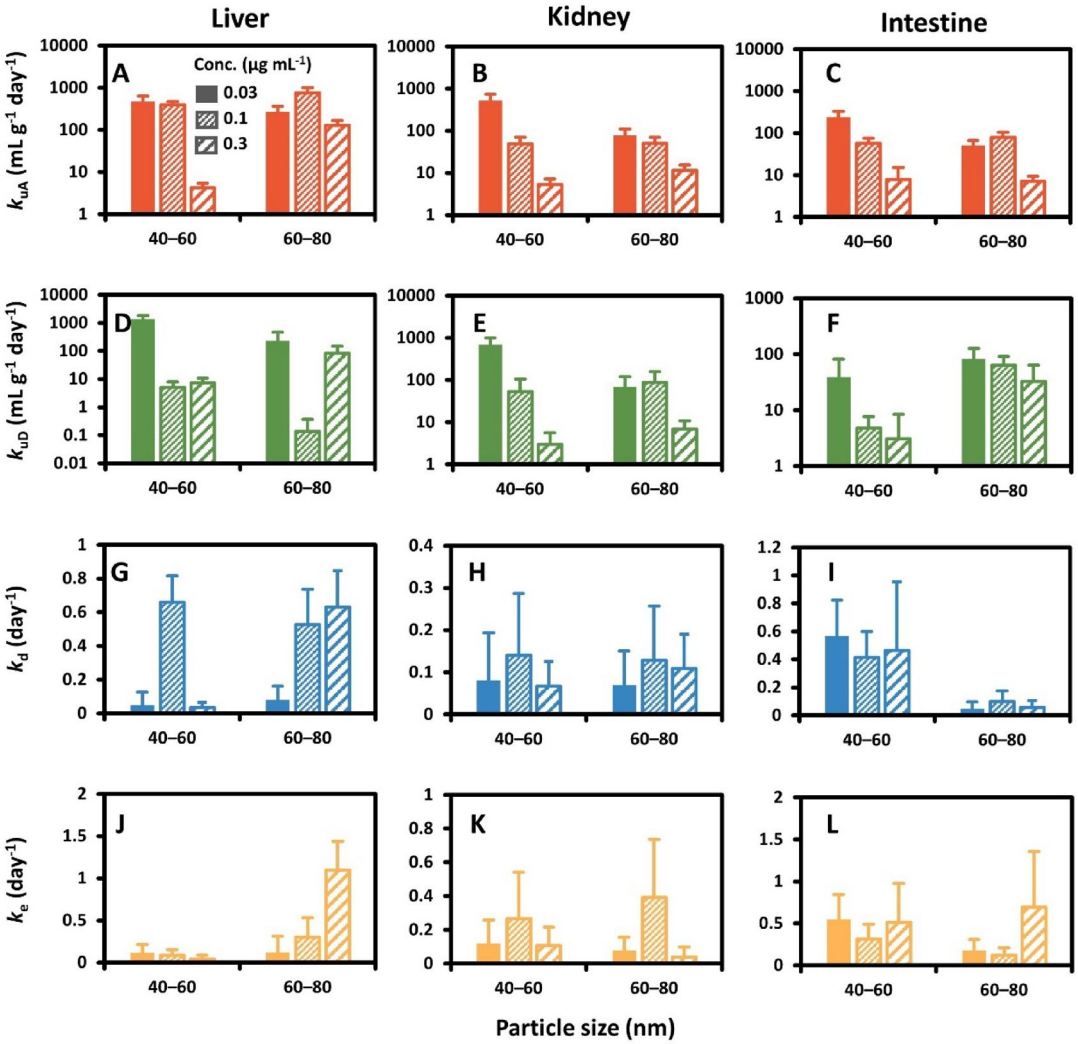

Fig. 3. Posterior distributions (mean ± SD) of parameters updated in a two-compartment TK model with the Bayesian approach using CuNP subcellular data from (**A**, **D**, **G**, **J**) liver, (**B**, **E**, **H**, **K**) kidney and (**C**, **F**, **I**, **L**) intestine. Bar colors represent different kinetic parameters: red (uptake rate of the MAP, k_{uA}), green (uptake rate of the MDP, k_{uD}), blue (detoxification rate, k_d), and yellow (elimination rate, k_e). Solid and hatched bars correspond to exposure concentrations of 0.03, 0.1, and 0.3 μg mL^{-1}, as indicated in the legend.

exposure concentrations, smaller-sized CuNPs did not affect greater Cu accumulation in either the MAP or the MDP. The relative proportions of Cu distribution into MAP, MDP, and cellular debris further support the detoxification role of MDP, especially under exposure to smaller sized CuNPs (Fig. S6).

Multivariate analysis of partitioning and toxicokinetics

We further examined the effects of particle size and concentration on the toxicity and detoxification of CuNPs in three tissues. Principal components analysis (PCA) revealed that the principal components explain72.6%, 73.1%, and 65.4% of the total variability in the livers, kidneys, and intestines respectively (Fig. 6). Dimension 2 of the PCA clearly distinguished Cu accumulation between exposure to small- and large-sized CuNPs. For the liver and intestine, exposure to the small-sized CuNPs was closely related to the proportion of Cu in MDP (% MDP) (Fig. 6A, B, E, F). Conversely, the influence of larger-sized CuNPs on the kidneys correlated with the proportion of Cu concentration in MAP (% MAP) (Fig. 6C, D). Additionally, we used toxicokinetic parameters to assess variability in Cu accumulation across particle sizes, exposure concentrations, and tissues. Hierarchical clustering analyses indicated no significant toxicokinetic variability between particle size treatments, and the toxicokinetic function of the livers showed high similarity to those of the intestines (Fig. S7). The k_{uD} in all three tissues was distinctly grouped according to small-size and large-size CuNP exposures. The detoxification rate constant (k_d) and elimination rate constant (k_e) were also separated similarly by particle size. These findings suggest that particle size significantly influences the detoxification and elimination capacities.

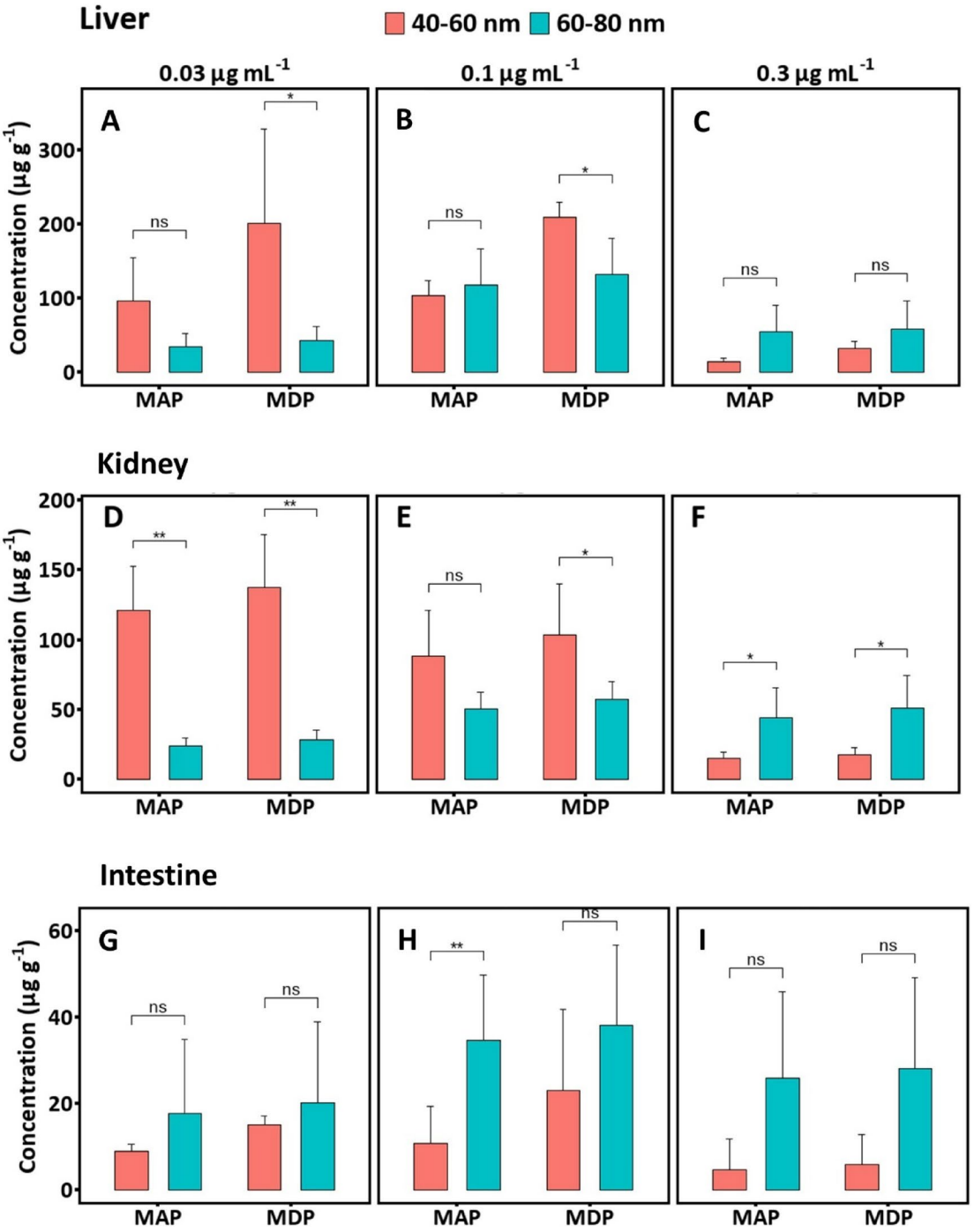

Fig. 4. Comparison of the effects of exposure to different sizes of CuNPs on copper accumulation in the MAP and the MDP across various tissues: (**A**–**C**) liver, (**D**–**F**) kidney, and (**G**–**I**) intestine. Red bars represent 40–60 nm CuNPs and blue bars represent 60–80 nm CuNPs. Data are shown as mean ± SD ($n = 5$). Statistical tests: t-test for liver and kidney; Mann–Whitney U-test for intestine. Statistical significance is indicated as $^{*}p < 0.05$, $^{**}p < 0.01$, $^{***}p < 0.001$, and ns = not significant.

Discussion

Effects of particle size and concentration on toxicokinetics

This study indicates that smaller CuNP sizes (40–60 nm), combined with lower to moderate exposure concentrations, are associated with higher Cu accumulation in the kidneys and liver of grass carp. Particle size plays a pivotal role in chemical absorption and subsequent biological effects. Specifically, smaller particles possess a larger surface area relative to their volume, leading to quicker dissolution in aquatic environments. Previous studies reported that 50-nm CuNPs released approximately 41% of their Cu ions within 24 h, compared

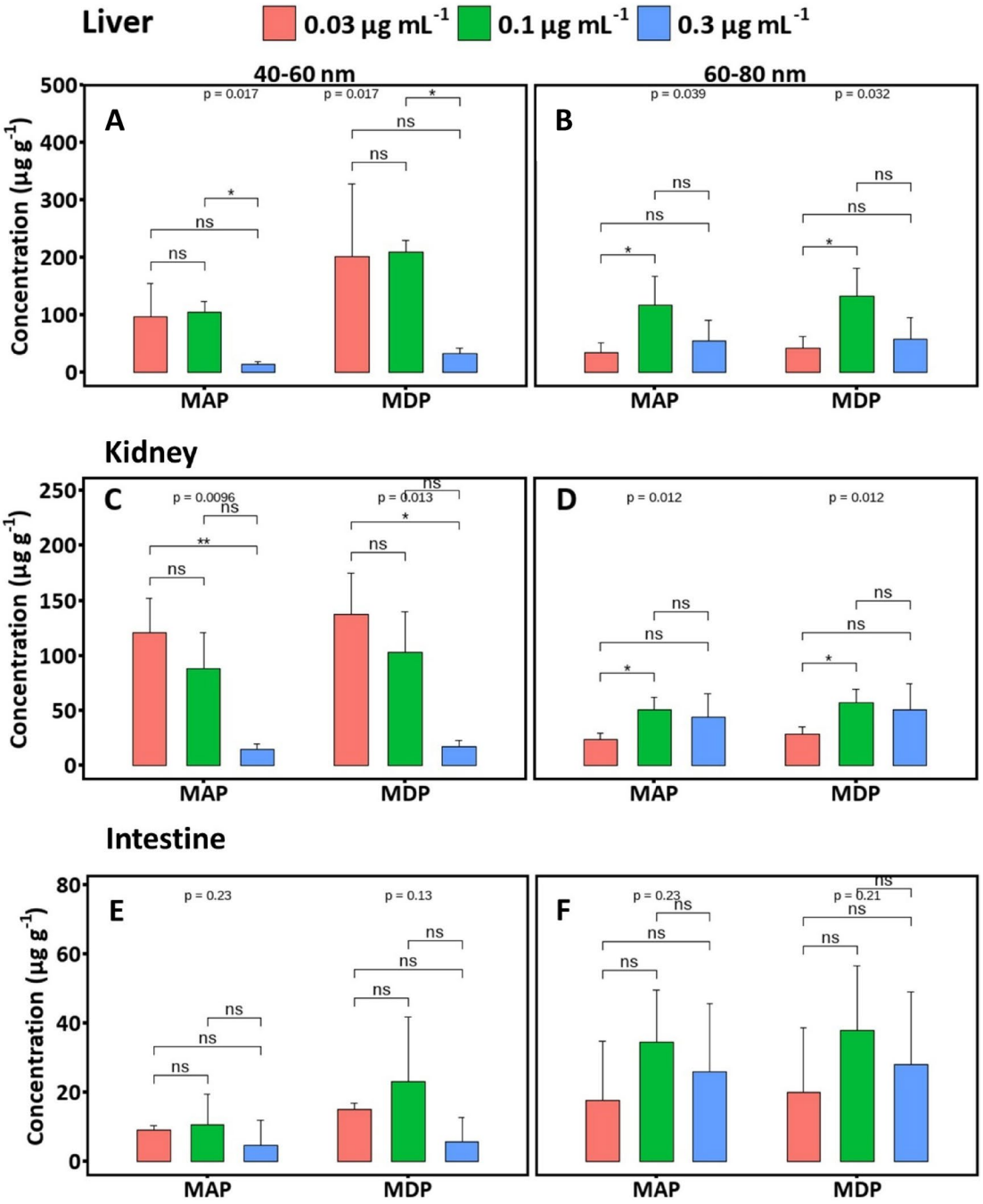

Fig. 5. Comparison of the effects of different concentrations of CuNP exposure on copper accumulation in the MAP and the MDP across various tissues: (**A**, **B**) liver, (**C**, **D**) kidney, and (**E**, **F**) intestine. Red, green, and blue bars represent CuNP concentrations of 0.03, 0.1, and 0.3 µg mL^{-1}, respectively. Data are shown as mean ± SD ($n = 5$). Statistical tests: Kruskal-Wallis test for liver and kidney in the 40–60 nm treatments, and for intestine; ANOVA for liver and kidney in the 60–80 nm treatments. Statistical differences between concentrations are indicated with $^{*}p < 0.05$, $^{**}p < 0.01$, $^{***}p < 0.001$, and ns = not significant.

to only 23% released by 78-nm CuNPs under similar conditions[45,46]. This increased dissolution not only enhances bioavailability but also elevates toxicity through chemical oxidation processes, particularly in copper oxide[47]. Our findings reveal that smaller sizes of CuNPs, ranging from 40 to 60 nm, affect the linear increase in Cu accumulation in the MAP of the kidneys and liver, indicating a dual process of toxicological impact and detoxification response. Notably, this aligns with prior research demonstrated that smaller-sized CuNPs exhibited significantly higher toxicity compared to bulk CuO, with toxicity increase ranging from 40- to 50-fold[48–50]. This heightened toxicity is attributed to the substantial release of Cu ions from smaller CuNPs, which are more reactive and bioavailable. However, it is important to note that nanoparticle-induced toxicity extends beyond

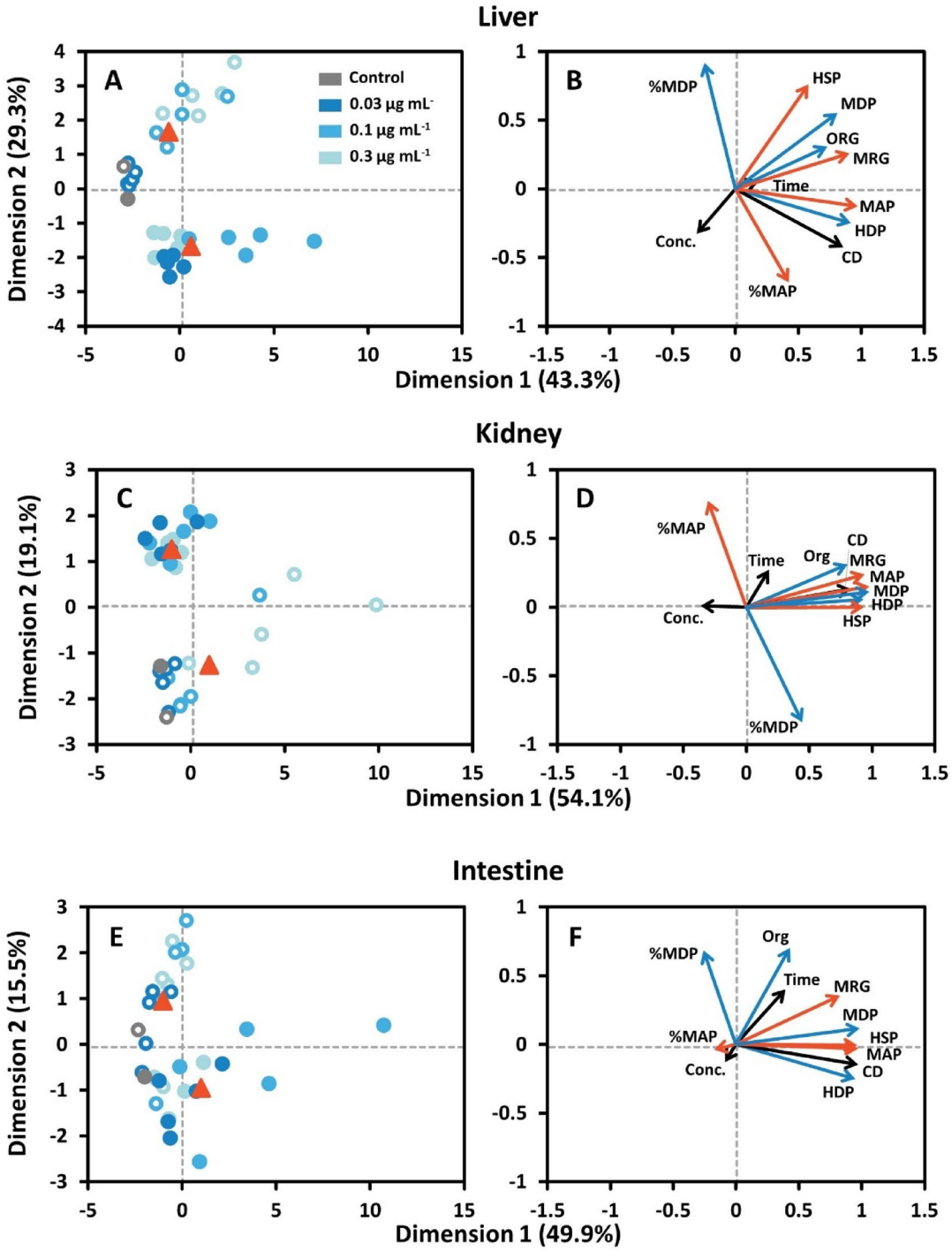

Fig. 6. PCA plots for examining the correlation among Cu concentrations in different subcellular partitioning in (**A**, **B**) liver, (**C**, **D**) kidney, and (**E**, **F**) intestine of grass crap exposed to 0.03, 0.1, and 0.3 μg mL^{-1} CuNPs of 40–60 (hollow spot) and 60–80 nm (solid spot). The triangle points in (**A**, **C**, and **E**) represent the center of the PCA groups.

size-dependent dissolution. Baek and An[51] demonstrated that Cu nanotoxicity arises not only from dissolved Cu but also from direct effects of intact nanoparticles. While metal ions may be more readily distributed to the metabolically active pool[20], intact particles are more likely to be sequestered in the metabolically detoxified pool, as part of the subcellular strategy to isolate and neutralize potentially harmful particles[52]. In this study, we measured total Cu concentrations without distinguishing between particle and ionic forms. The extent to which the accumulated Cu originated from intact nanoparticles or from dissolved Cu ions remains uncertain. This distinction is important, as ionic Cu and CuNPs may exhibit different bioavailability and toxicity. Advanced techniques such as single-particle ICP-MS and X-ray absorption spectroscopy can differentiate between

nanoparticle and ionic forms of Cu and better understand the contributions to accumulation and toxicity[53,54]. Additionally, the characteristics of CuNPs, including shape, surface charge, and aggregation behavior, significantly influence their distribution, toxicity, and interactions with biological systems. For example, nanoparticle aggregation in different environments, such as water, plasma, and cellular compartments, alter their surface properties and bioactivity[55–58]. While this study quantitative confirmed particle aggregation and size distribution in suspension, it did not include quantitative analyses in the actual exposure medium, where such measurements are challenging at low exposure concentrations[28]. This limitation is important, as quantitative characterization would enhance a clear understanding of nanoparticle behavior under environmentally relevant conditions. These findings underscore the complexity of CuNP on accumulation and toxicity, which is not solely governed by particle size but also modulated by nanoparticle-specific characteristics and environmental factors. Therefore, a comprehensive understanding of these interactions is essential for accurately assessing the risks associated with CuNP exposure.

Although the study design included three CuNP exposure concentrations to establish quantitative, concentration-dependent toxicokinetic parameters, the results did not demonstrate monotonic trends across tissues or subcellular. In particular, Cu accumulation decreased or plateaued at higher concentrations in smaller-sized CuNPs. In light of these patterns, we emphasized qualitative comparisons to interpret the influence of particle size, exposure level, and tissues on subcellular partitioning and bioavailability. Lower Cu accumulation was observed in fish exposed to smaller-sized CuNP at higher concentrations, whereas higher Cu accumulation was observed at lower concentrations of smaller-sized CuNPs. Specifically, at high concentrations, we observed reduced Cu accumulations in the MAP of the kidneys and livers of grass carp, particularly for small-sized CuNP. This aligns with our toxicokinetic findings, which show that the uptake rates in both MAP and MDP compartments decreased as exposure concentration increased, particularly for smaller particles. However, these results differ from the findings of Zhao and Wang[11], who reported that the influx rate of small silver nanoparticles continued to increase at higher concentrations during short-term exposure. This discrepancy could be explained by the aggregation behavior of nanoparticles in the external environment. In particular, environmental factors such as dissolved organic matter, pH, ionic strength, and divalent cation concentrations influence the aggregation behavior of metallic nanoparticles in aquatic systems, with low pH and high divalent cation concentration exerting the strongest effect[59–62]. The stability of CuNPs is also affected by the salinity and pH of natural waters, with smaller particles that tend to remain suspended under high salinity conditions[63]. However, our study did not include actual concentrations of CuNP in the experimental exposure solution and nanoparticle characteristic in the actual exposure medium, which limits the ability to provide environmentally relevant information about the bioavailability of CuNPs. Both particle size and concentration strongly influence aggregation dynamics. Although actual CuNP concentrations in the exposure tanks were not determined, we measured total Cu concentration in fish culture medium at nominal concentration of 0.1–1 mg L^{-1} CuNPs. These results indicated greater losses for larger particles (60–80 nm, 0.008–0.348 mg L^{-1}) relative to smaller particles (40–60 nm, 0.060–0.700 mg L^{-1}), which is consistent with finding that particle size strongly affects dissolved Cu concentrations in exposure media[64]. At 100 mg L^{-1} of CuNPs, the dissolved Cu concentration for 40 nm CuNPs was ~ 0.1 mg L^{-1} in daphnia culture medium and ~ 0.6 mg L^{-1} in deionized water, while 25 nm CuNPs reached ~ 1.0 mg L^{-1} in both media. For instance, higher exposure concentrations of nanoparticles are rapid and extensively promote aggregation compared to lower exposure concentrations[65,66], particularly in small-sized nanoparticles[67]. Hua et al.[66] further demonstrated that 50-nm CuNPs exhibited an approximately 18-fold increase in aggregation under high concentrations, compared to only a 6.5-fold increase for 100-nm CuNP, with no discernible influence from concentration variations in larger particles. The aggregation of small-sized CuNP in water leads to several downstream effects, including a reduction of waterborne copper concentrations by over 86% compared to the initial exposure concentration and an increase in nanoparticle size[57,68], which affects cellular uptake. Consequently, under high-concentration exposure, smaller-sized CuNPs influence lower bioavailability and reduced Cu accumulation in tissues of grass carp. These results demonstrate that nanoparticle aggregation may limit metal uptake under environmentally realistic high-concentration scenarios. This finding underscores the importance of considering particle size, concentration, and aggregation-related reduction in bioavailability in determining the toxicokinetic and toxicodynamic outcomes of CuNP exposure. While high toxicity could potentially impair physiological functions and reduce uptake, no abnormal physiological behaviors were observed in any treatment group during the exposure period. We interpret that under the tested concentrations, CuNP exposure did not induce overt physiological stress that would interfere with normal uptake processes. Therefore, the reduced Cu accumulation observed at higher CuNP concentrations is more plausibly attributed to nanoparticle aggregation and related to decreased bioavailability. Previous studies showed increased nanoparticle concentrations promote particle aggregation, limiting cellular uptake[65,66,69].

Tissues detoxification kinetics and implications for risk assessment

Our study revealed a significant Cu accumulation in the intestines over time following waterborne exposure, consistent with previous research demonstrating CuNP exposure in goldfish (*Carassius auratus*) and carp (*Cyprinus carpio*) via the waterborne route[7,29]. These findings highlight the role of waterborne CuNP exposure as a pathway for Cu accumulation in the intestines through internalization across the gills. Exposure to smaller particle sizes of CuNPs notably increased the Cu accumulation in the liver and intestinal MDPs, suggesting their involvement in storage and detoxification mechanisms. Moreover, CuNPs achieve Cu concentration equilibrium more rapidly in the liver and intestinal MAP, suggesting minimal concerns regarding toxicity during exposure. To further illustrate the pathway of CuNP absorption and tissue-specific distribution, a conceptual flowchart depicting the transport among the intestine, liver, and kidney has been shown in Fig. S8. Scola et al.[19] indicated that the bivalve *Scrobicularia plana* mitigates CuNP toxicity by sequestering Cu into metal-rich granules and upregulating protective proteins like metallothionein, thereby promoting detoxification. Similarly, the fish liver

plays a critical role in both storing and metabolizing Cu, particularly metallothionein-mediate pathways[70]. Additionally, Wang et al.[71] found that HSP 70 and HSP 90 were upregulated in the intestines of *Epinephelus coioides* during CuNP exposure, facilitating apoptosis regulation and enhancing the detoxification mechanism. Incorporating detoxification rate (k_d) into toxicokinetic frameworks allows for the prediction of metal retention and long-term toxicity under different exposure conditions and the development of more accurate environmental risk assessment models.

In the toxicokinetic framework of subcellular partitioning, which includes two uptake rates and detoxification rate. The uptake rate k_{uA} respesents the transfer of Cu into MAP, which is associated with toxic effects. In contrast, k_{uD} describes the rate of uptake into MDP, reflecting storage and detoxification mechanisms. The detoxification rate (k_d) characterizes the ability to migrate toxicity by transferring Cu from the MAP to the MDP. The relative magnitudes of k_{uA} and k_{uD} indicate the balance between toxic burden and detoxification capacity in tissues. For instance, a higher proportion of Cu accumulates in the active pool relative to detoxification pathways in k_{uA} exceeds k_{uD}, implying the potential for causing toxic stress. In the case of smaller CuNP sizes, observed toxicity in the intestines (i.e., $k_{uA} > k_{uD}$), is mitigated through the detoxification rate (k_d), which facilitates the transfer of Cu from the MAP to the MDP for detoxification. Conversely, in the liver, toxicity becomes apparent in larger particle sizes (also characterized by $k_{uA} > k_{uD}$), although detoxification rates (k_d) consistently increase with exposure concentration. Our results show that the intestines and liver detoxification capacities are primarily governed by the transfer rate of Cu from MAP to MDP. Tissue-specific toxicokinetics and detoxification in subcellular processes should be considered in CuNP risk assessments. The toxicokinetic model of subcellular partitioning provides important insights by (i) linking the exposure characteristic in nanoparticle size and concentration of CuNP with the biodistribution pattern, and (ii) tissue-specific physiological function influence accumulation, transformation, and detoxification dynamics of CuNPs. This model provides a quantitative basis for toxicological risk assessment and emphasizes that the differences in uptake and detoxification reflect the intrinsic defense capacities of different tissues under nanoparticle-induced stress.

Studies on Cu accumulation and detoxification kinetics in fish tissues in response to CuNP exposure remain limited, posing challenges in directly comparing activation and detoxifying rates. The finding that detoxification capacity varies by particle size and tissue type highlights the importance of considering organism-level defense mechanisms in environmental risk assessments. By quantifying Cu redistribution from MAP to MDP, our approach provides a mechanistic basis for refining toxicokinetic models to reflect real-world exposure and biological response scenarios better.

Hampton et al.[72] demonstrated that vesicles can reach diameters of up to 200 nm, indicating that the excretion of CuNPs from the liver is feasible. Additionally, the reabsorption of Cu metallothionein in the liver, followed by the synthesis of thionein in the kidneys, contributes to the eventual accumulation of Cu in the kidneys[73]. The tissue-level redistribution processes and initial uptake play an important role in long-term metal accumulation patterns. Nanoparticle kinetics of uptake and excretion are not solely influenced by particle size but also by interactions with cellular or protein elements, such as the protein corona, within physiological environments[74]. Larger nanoparticles tend to attract proteins with higher molecular weights in biological fluids, while smaller nanoparticles predominantly interact with lower molecular weight proteins on their surfaces[75]. These protein-nanoparticle interactions can moderate nanoparticle behavior in biological fluids, potentially affecting internal bioavailability and detoxification efficiency[76,77]. Although this study did not directly examine protein corona formation, such interactions may partly explain the observed tissue-specific accumulation pattern and kinetic differences. Not only particle size but also protein corona formation and other characteristics influence detoxification and activation processes in aquatic organisms. This highlights a knowledge gap in understanding how physicochemical properties modulate subcellular toxicokinetics. Overall, integrating subcellular partitioning kinetics into ecotoxicological models enhances the model capacity to simulate organismal responses under varying nanoparticle exposure scenarios. This approach provides a pathway for developing predictive, physiologically relevant risk frameworks that bridge the gap between experimental ecotoxicology and environmental management.

Conclusions

The Bayesian inference subcellular partitioning TK model provided robust estimations of toxicokinetic parameters, revealing differential uptake and detoxification rates across tissues and particle sizes. Notably, smaller particle sizes are associated with enhanced detoxification rates, a quick transfer of Cu to the MDP for storage and elimination in the intestines and liver. It is worth mentioning that higher concentrations of small-sized CuNPs did not consistently increase Cu accumulation in tissues, suggesting the possibility of aggregation effects or altered uptake mechanisms. Thus, the interaction between particle size and concentration underscores the dynamic complexity of CuNPs in aquatic organisms, in which higher concentrations can alter accumulation patterns and toxicity profiles despite particle size effects. Overall, our findings highlight the importance of considering both particle characteristics and exposure levels in assessing the environmental risks and biological responses associated with CuNP exposure in aquatic ecosystems.

Data availability

The data from this study are available from the corresponding author upon reasonable request.

Received: 7 April 2025; Accepted: 8 October 2025
Published online: 14 November 2025

References

1. Wei, C. & Liu, Q. Shape-, size-, and density-tunable synthesis and optical properties of copper nanoparticles. *Cryst. Eng. Comm.* **19**(24), 3254–3262 (2017).
2. Asghar, M. et al. Comparative analysis of synthesis, characterization, antimicrobial, antioxidant, and enzyme Inhibition potential of roses petal based synthesized copper oxide nanoparticles. *Mater. Chem. Phys.* **278**, 125724 (2022).
3. Adam, V., Wu, Q. & Nowack, B. Integrated dynamic probabilistic material flow analysis of engineered materials in all European countries. *NanoImpact* **22**, 100312 (2021).
4. Garner, K. L., Suh, S. & Keller, A. A. Assessing the risk of engineered nanomaterials in the environment: development and application of the nanofate model. *Environ. Sci. Technol.* **51**(10), 5541–5551 (2017).
5. Adeleye, A. S., Oranu, E. A., Tao, M. & Keller, A. A. Release and detection of nanosized copper from a commercial antifouling paint. *Water Res.* **102**, 374–382 (2016).
6. Keller, A. A. et al. Comparative environmental fate and toxicity of copper nanomaterials. *NanoImpact* **7**, 28–40 (2017).
7. Zhao, J. et al. Distribution of CuO nanoparticles in juvenile carp (*Cyprinus carpio*) and their potential toxicity. *J. Hazard. Mater.* **197**, 304–310 (2011).
8. Kalman, J. et al. Bioaccumulation of CuO nanomaterials in rainbow trout: influence of exposure route and particle shape. *Chemosphere* **310**, 136894 (2023).
9. Kang, J. S. & Park, J. W. Insight on cytotoxic effects of silver nanoparticles: alternative androgenic transactivation by adsorption with DHT. *Sci. Total Environ.* **618**, 712–717 (2018).
10. Perde-Schrepler, M. et al. Size-dependent cytotoxicity and genotoxicity of silver nanoparticles in cochlear cells in vitro. *J. Nanomater.* 6090259 (2019).
11. Zhao, C. M. & Wang, W. X. Size-dependent uptake of silver nanoparticles in *Daphnia magna*. *Environ. Sci. Technol.* **46**(20), 11345–11351 (2012).
12. Kaya, H. et al. Effects of zinc oxide nanoparticles on bioaccumulation and oxidative stress in different organs of tilapia (*Oreochromis niloticus*). *Environ. Toxicol. Pharmacol.* **40**(3), 936–947 (2015).
13. Mehennaoui, K. et al. Do the pristine physico-chemical properties of silver and gold nanoparticles influence uptake and molecular effects on *Gammarus fossarum* (Crustacea Amphipoda)? *Sci. Total Environ.* **643**, 1200–1215 (2018).
14. Burello, E. & Worth, A. P. A theoretical framework for predicting the oxidative stress potential of oxide nanoparticles. *Nanotoxicology* **5**(2), 228–235 (2011).
15. Rocha, T. L., Gomes, T., Durigon, E. G. & Bebianno, M. J. Subcellular partitioning kinetics, metallothionein response and oxidative damage in the marine mussel *Mytilus galloprovincialis* exposed to cadmium-based quantum Dots. *Sci. Total Environ.* **554**, 130–141 (2016).
16. Yan, C. et al. Changes in arsenate bioaccumulation, subcellular distribution, depuration, and toxicity in *Artemia Salina* nauplii in the presence of titanium dioxide nanoparticles. *Environ. Sci. Nano*. **4**(6), 1365–1376 (2017).
17. Fan, W., Li, Q., Yang, X. & Zhang, L. Zn subcellular distribution in liver of goldfish (*Carassius auratus*) with exposure to zinc oxide nanoparticles and mechanism of hepatic detoxification. *PLoS ONE*. **8**(11), e78123 (2013).
18. Beaumelle, L., Hedde, M., Vandenbulcke, F. & Lamy, I. Relationships between metal compartmentalization and biomarkers in earthworms exposed to field-contaminated soils. *Environ. Pollut.* **224**, 185–194 (2017).
19. Scola, S., Blasco, J. & Campana, O. Nanosize effect in the metal-handling strategy of the bivalve *Scrobicularia plana* exposed to CuO nanoparticles and copper ions in whole-sediment toxicity tests. *Sci. Total Environ.* **760**, 143886 (2021).
20. Wallace, W. G., Lee, B. G. & Luoma, S. N. Subcellular compartmentalization of cd and Zn in two bivalves. I. Significance of metal-sensitive fractions (MSF) and biologically detoxified metal (BMD). *Mar. Ecol. Prog Ser.* **249**, 183–197 (2003).
21. Manke, A., Wang, L. & Rojanasakul, Y. Mechanisms of nanoparticle-induced oxidative stress and toxicity. *Biomed. Res. Int.* **2013**, 942916 (2013).
22. Chen, W. Y. Toxicokinetic modeling challenges for aquatic nanotoxicology. *Front. Mar. Sci.* **2**, 114 (2016).
23. McNally, K. et al. Reconstruction of exposure to m-xylene from human biomonitoring data using PBPK modeling, Bayesian inference, and Markov Chain Monte Carlo simulation. *J. Toxicol.* **2012**(1), 760281 (2012).
24. Sweeney, L. M., MacCalman, L., Haber, L. T., Kuempel, E. D. & Tran, C. L. Bayesian evaluation of a physiologically-based pharmacokinetic (PBPK) model of long-term kinetics of metal nanoparticles in rats. *Regul. Toxicol. Pharmacol.* **73**(1), 151–163 (2015).
25. Lin, H. C. & Chen, W. Y. Bayesian population physiologically-based Pharmacokinetic model for robustness evaluation of withdrawal time in tilapia aquaculture administrated to florfenicol. *Ecotoxicol. Environ. Saf.* **210**, 111867 (2021).
26. Chou, W. C. et al. Development of a multi-route physiologically based pharmacokinetic (PBPK) model for nanomaterials: a comparison between a traditional versus a new route-specific approach using gold nanoparticles in rats. *Part. Fibre Toxicol.* **19** (1), 47 (2022).
27. Prabhu, B. M., Ali, S. F., Murdock, R. C., Hussain, S. M. & Srivatsan, M. Copper nanoparticles exert size and concentration dependent toxicity on somatosensory neurons of rat. *Nanotoxicology* **4**(2), 150–160 (2010).
28. Shaw, B. J., Al-Bairuty, G. & Handy, R. D. Effects of waterborne copper nanoparticles and copper sulphate on rainbow trout (*Oncorhynchus mykiss*): Physiology and accumulation. *Aquat. Toxicol.* **116–117**, 90–101 (2012).
29. Ates, M., Arslan, Z., Demir, V., Daniels, J. & Farah, I. O. Accumulation and toxicity of CuO and ZnO nanoparticles through waterborne and dietary exposure of goldfish (*Carassius auratus*). *Environ. Toxicol.* **30**(1), 119–128 (2015).
30. Wang, J. & Mao, L. Lethal time and histological changes in starved common carp, silver carp, bighead carp and grass carp fry and fingerlings. *J. Dalian Fish. Univ.* **8**, 59–65 (1993).
31. Al-Bairuty, G. A., Shaw, B. J., Handy, R. D. & Henry, T. B. Histopathological effects of waterborne copper nanoparticles and copper sulphate on the organs of rainbow trout (*Oncorhynchus mykiss*). *Aquat. Toxicol.* **126**, 104–115 (2013).
32. Percie du Sert, N. et al. The ARRIVE guidelines 2.0: Updated guidelines for reporting animal research. *BMC Vet. Res.* **16**, 242 (2020).
33. Geffard, A. et al. Subcellular compartmentalization of cadmium, nickel, and lead in *Gammarus fossarum*: Comparison of methods. *Chemosphere* **78**, 822–829 (2010).
34. Rainbow, P. S. Trace metal concentrations in aquatic invertebrates: Why and so what? *Environ. Pollut*. **120**(3), 497–507 (2002).
35. Mason, A. Z. & Jenkins, K. D. Metal detoxification in aquatic organisms. in *Metal Speciation and Bioavailability in Aquatic Systems* (eds Tessier, A. & Turner, D.) 479–608 J. Wiley & Sons, Chichester, UK, 1995).
36. George, S. G. & Olsson, P. E. Metallothionein as indicators of trace metal pollution. in *Biomonitoring of Coastal Waters and Estuaries* (ed Kramer, K. J. M.) 151–178 (CRC, Boca Raton,1994).
37. Andrews, G. K. Regulation of metallothionein gene expression by oxidative stress and metal ions. *Biochem. Pharmacol.* **59**, 95–104 (2000).
38. Ivanković, D., Pavičić, J., Beatović, V., Klobučar, R. S. & Klobučar, G. Inducibility of metallothionein biosynthesis in the whole soft tissue of zebra mussels *Dreissena polymorpha* exposed to cadmium, copper, and pentachlorophenol. *Environ. Toxicol.* **25**(2), 198–211 (2010).
39. Nassiri, Y., Rainbow, P. S., Amiard-Triquet, C., Rainglet, F. & Smith, B. D. Trace metal detoxification in the ventral caeca of *Orchestia Gammarellus* (Crustacea: Amphipoda). *Mar. Biol.* **136**, 477–484 (2000).
40. Gelman, A. & Rubin, D. B. Inference from iterative simulation using multiple sequences. *Stat. Sci.* **7**(4), 457–472 (1992).

41. Kim, S. & Kim, H. A new metric of absolute percentage error for intermittent demand forecasts. *Int. J. Forecast.* **32**(3), 669–679 (2016).
42. Moreno, J. J. M., Pol, A. P., Abad, A. S. & Blasco, B. C. Using the R-MAPE index as a resistant measure of forecast accuracy. *Psicothema* **25**(4), 500–506 (2013).
43. Husson, F., Josse, J., Le, S. & Mazet, J. FactoMineR: Multivariate exploratory data analysis and data mining. *R Package Version* **2**, 4 (2020).
44. Kassambara, A., Mundt, F. & Factoextra Extract and Visualize the Results of Multivariate Data Analyses. R Package Version 1.0.7 (2020).
45. Zhang, L. & Wang, W. X. Dominant role of silver ions in silver nanoparticle toxicity to a unicellular alga: Evidence from luminogen imaging. *Environ. Sci. Technol.* **53**, 494–502 (2019).
46. Song, L. et al. Species-specific toxicity of copper nanoparticles among mammalian and piscine cell lines. *Nanotoxicology* **8**(4), 383–393 (2014).
47. Sajjad, H., Sajjad, A., Haya, R. T., Khan, M. M. & Zia, M. Copper oxide nanoparticles: In vitro and in vivo toxicity, mechanisms of action and factors influencing their toxicology. *Comp. Biochem. Physiol. C Toxicol. Pharmacol.* **271**, 109682 (2023).
48. Kaweeteerawat, C. et al. Cu nanoparticles have different impacts in *Escherichia coli* and *Lactobacillus brevis* than their microsized and ionic analogues. *ACS Nano* **9**(7), 7215–7225 (2015).
49. Lin, S. et al. Understanding the transformation, speciation, and hazard potential of copper particles in a model septic tank system using zebrafish to monitor the effluent. *ACS Nano*. **9**(2), 2038–2048 (2015).
50. Gunawan, C., Teoh, W. Y., Marquis, C. P. & Amal, R. Cytotoxic origin of copper (II) oxide nanoparticles: comparative studies with micron-sized particles, leachate, and metal salts. *ACS Nano* **5**, 7214–7225 (2011).
51. Baek, Y. W. & An, Y. J. Microbial toxicity of metal oxide nanoparticles (CuO, NiO, ZnO, and Sb2O3) to *Escherichia coli*, *Bacillus subtilis*, and *Streptococcus aureus*. *Sci. Total Environ.* **409**, 1603–1608 (2011).
52. Luoma, S. N. & Rainbow, P. S. Why is metal bioaccumulation so variable? Biodynamics as a unifying concept. *Environ. Sci. Technol.* **39**(7), 1921–1931 (2005).
53. Laborda, F., Bolea, E. & Jiménez-Lamana, J. Single particle inductively coupled plasma mass spectrometry: A powerful tool for nanoanalysis. *Anal. Chem.* **86**(5), 2270–2278 (2014).
54. Godfrey, I. J., Dent, A. J., Parkin, I. P., Maenosono, S. & Sankar, G. Following the formation of silver nanoparticles using in situ x-ray absorption spectroscopy. *ACS Omega* **5**(23), 13664–11367 (2020).
55. Misra, S. K. et al. Comparative study using spheres, rods and spindle-shaped nanoplatelets on dispersion stability, dissolution and toxicity of CuO nanomaterials. *Nanotoxicology* **8**, 422–432 (2014).
56. Costa, P. M. et al. Transcriptional profiling reveals gene expression changes associated with inflammation and cell proliferation following short-term inhalation exposure to copper oxide nanoparticles. *J. Appl. Toxicol.* **38**, 385–397 (2018).
57. Pereira, S. P., Boyle, D., Nogueira, A. & Handy, R. D. Differences in toxicity and accumulation of metal from copper oxide nanomaterials compared to copper sulphate in zebrafish embryos: Delayed hatching, the chorion barrier and physiological effects. *Ecotoxicol. Environ. Saf.* **253**, 114613 (2023).
58. Corbo, C. et al. The impact of nanoparticle protein corona on cytotoxicity, immunotoxicity and target drug delivery. *Nanomedicine* **11**(1), 81–100 (2016).
59. Adeleye, A. S., Conway, J. R., Perez, T., Rutten, P. & Keller, A. A. Influence of extracellular polymeric substances on the long-term fate, dissolution, and speciation of copper-based nanoparticles. *Environ. Sci. Technol.* **48**(21), 12561–12568 (2014).
60. Conway, J. R., Adeleye, A. S., Gardea-Torresdey, J. & Keller, A. A. Aggregation, dissolution, and transformation of copper nanoparticles in natural waters. *Environ. Sci. Technol.* **49**(5), 2749–2756 (2015).
61. Peng, Y. H., Tsai, Y. C., Hsiung, C. E., Lin, Y. H. & Shih, Y. H. Influence of water chemistry on the environmental behaviors of commercial ZnO nanoparticles in various water and wastewater samples. *J. Hazard. Mater.* **322**(Pt B), 348–356 (2017).
62. Xiao, Y., Vijver, M. G. & Peijnenburg, W. J. G. M. Impact of water chemistry on the behavior and fate of copper nanoparticles. *Environ. Pollut.* **234**, 684–691 (2018).
63. Torres-Duarte, C. et al. Developmental effects of two different copper oxide nanomaterials in sea urchin (*Lytechinus pictus*) embryos. *Nanotoxicology* **10**(6), 671–679 (2016).
64. Santos-Rasera, J. R., Neto, A. S. A., Monteiro, R. T. R., Van Gestel, C. A. & De Carvalho, H. W. P. Toxicity, bioaccumulation and biotransformation of Cu oxide nanoparticles in *Daphnia magna*. *Environ. Science: Nano*. **6**(9), 2897–2906 (2019).
65. Nel, A. E. et al. Understanding biophysicochemical interactions at the nano-bio interface. *Nat. Mater.* **8**, 543–557 (2009).
66. Hua, J., Vijver, M. G., Ahmad, F., Richardson, M. K. & Peijnenburg, W. J. Toxicity of different-sized copper nano- and submicron particles and their shed copper ions to zebrafish embryos. *Environ. Toxicol. Chem.* **33**(8), 1774–1782 (2014).
67. Sun, H., Jiao, R., An, G., Xu, H. & Wang, D. Influence of particle size on the aggregation behavior of nanoparticles: Role of structural hydration layer. *J. Environ. Sci.* **103**, 33–42 (2021).
68. Tesser, M. E. et al. Sublethal effects of waterborne copper and copper nanoparticles on the freshwater neotropical teleost *Prochilodus lineatus*: A comparative approach. *Sci. Total Environ.* **704**, 135332 (2020).
69. Canta, M. & Cauda, V. The investigation of the parameters affecting the ZnO nanoparticle cytotoxicity behaviour: A tutorial review. *Biomater. Sci.* **8**(22), 6157–6174 (2020).
70. Grosell, M. H., Hogstrand, C. & Wood, C. M. Renal Cu and Na excretion and hepatic Cu metabolism in both Cu acclimated and non-acclimated rainbow trout (*Oncorhynchus mykiss*). *Aquat. Toxicol.* **40**, 275–291 (1998).
71. Wang, T., Long, X., Liu, Z., Cheng, Y. & Yan, S. Effect of copper nanoparticles and copper sulphate on oxidation stress, cell apoptosis and immune responses in the intestines of juvenile *Epinephelus coioides*. *Fish. Shellfish Immunol.* **44**(2), 674–682 (2015).
72. Hampton, J. A., Lantz, C., Goldblatt, R., Lauren, P. J., Hinton, D. E. & D. J. & Functional units in rainbow trout (*Salmo gairdneri*, Richardson) liver: II. The biliary system. *Anat. Rec.* **221**, 619–634 (1988).
73. Isani, G. et al. Comparative toxicity of CuO nanoparticles and $CuSO_4$ in rainbow trout. *Ecotoxicol. Environ. Saf.* **97**, 40–46 (2013).
74. Ault, A. P. et al. Protein corona-induced modification of silver nanoparticle aggregation in simulated gastric fluid. *Environ. Sci. Nano*. **3**(6), 1510–1522 (2016).
75. Mahmoudi, M. et al. Crucial role of the protein corona for the specific targeting of nanoparticles. *Nanomedicine* **10**(2), 215–226 (2015).
76. Gao, J., Lin, L., Wei, A. & Sepúlveda, M. S. Protein corona analysis of silver nanoparticles exposed to fish plasma. *Environ. Sci. Technol. Lett.* **4**(5), 174–179 (2017).
77. Barbalinardo, M., Caicci, F., Cavallini, M. & Gentili, D. Protein corona mediated uptake and cytotoxicity of silver nanoparticles in mouse embryonic fibroblast. *Small* **14**, e1801219 (2018).

Acknowledgements

This research was supported by the National Science and Technology Council in Taiwan under Grant MOST 103-2313-B-037-003, MOST 111-2628-E-024-001-MY3, and NSTC114-2221-E-204-002-MY3.

Author contributions

H.C.L. and W.Y.C. wrote the main manuscript text. H.C.L., C.W.L., and W.Y.C. performed the formal analysis and prepared figures and visualizations. Y.L.T., B.R.H., H.H.H., and T.H.L. conducted the experiments and contributed to validation. L.H.L. contributed to visualization and assisted in drafting the original text. WYC conceptualized the study, supervised the project, and acquired funding. All authors reviewed and approved the final manuscript.

Declarations

Competing interests

The authors declare no competing interests.

Additional information

Supplementary Information The online version contains supplementary material available at https://doi.org/10.1038/s41598-025-23730-4.

Correspondence and requests for materials should be addressed to W.-Y.C.

Reprints and permissions information is available at www.nature.com/reprints.

Publisher's note Springer Nature remains neutral with regard to jurisdictional claims in published maps and institutional affiliations.